

# 1 Dipole Pattern of Summer Ozone Pollution in the east of China and Its 2 Connection with Climate Variability

3 Xiaoqing Ma<sup>1</sup>, Zhicong Yin<sup>123</sup>

4 <sup>1</sup>Key Laboratory of Meteorological Disaster, Ministry of Education / Joint International Research Laboratory of  
5 Climate and Environment Change (ILCEC) / Collaborative Innovation Center on Forecast and Evaluation of  
6 Meteorological Disasters (CIC-FEMD), Nanjing University of Information Science & Technology, Nanjing  
7 210044, China

8 <sup>2</sup>Southern Marine Science and Engineering Guangdong Laboratory (Zhuhai), Zhuhai, China

9 <sup>3</sup>Nansen-Zhu International Research Centre, Institute of Atmospheric Physics, Chinese Academy of Sciences,  
10 Beijing, China

11 **Corresponding author:** Zhicong Yin (yinzhc@nuist.edu.cn)

12 **Address:** No. 219 Ningliu Road, Pukou District, Nanjing University of Information Science & Technology,  
13 Nanjing 210044, China

14 **Tel.:** (+86) 136 5516 1661

15

## 16 **Abstract.**

17 Surface O<sub>3</sub> pollution has become one of the most severe air pollution problems in China, which makes it of  
18 practical importance to understand O<sub>3</sub> variability. A south-north dipole pattern of summer-mean O<sub>3</sub> concentration  
19 in the east of China (DP-O<sub>3</sub>), which were centered at North China (NC) and the Pearl River Delta (PRD)  
20 respectively, has been identified from the simulation of a global 3-D chemical transport model for the period  
21 1980–2019. Large-scale anticyclonic (cyclonic) and cyclonic (anticyclonic) anomalies over NC and the PRD  
22 resulted in a sharp contrast of meteorological conditions between the above two regions. The enhanced (restrained)  
23 photochemistry in NC and restrained (enhanced) O<sub>3</sub> production in the PRD contributed to the DP-O<sub>3</sub>. Decreased  
24 sea ice anomalies near the Franz Josef Land and associated warm sea surface in May enhanced the Rossby-wave  
25 source over northern Europe and West Siberia, which eventually induced an anomalous Eurasia-like pattern to  
26 influence the formation of the DP-O<sub>3</sub>. The thermodynamic signals of the southern Indian Ocean dipole were stored  
27 in the subsurface and influenced spatial pattern of O<sub>3</sub> pollution in the east of China mainly through the Hadley  
28 circulation. The physical mechanisms behind the modulation of the atmospheric circulations and related DP-O<sub>3</sub>  
29 by these two climate anomalies at different latitudes were evidently verified by large-scale ensemble simulations  
30 of the earth system model.

31 **Key words:** ozone pollution; sea ice; Eurasia pattern; sea surface temperature; meridional circulation

## 32 1. Introduction

33 Surface O<sub>3</sub> is an important air pollutant. Exposure to high concentrations of O<sub>3</sub> is detrimental to both human  
34 health and vegetation ecology (Rider and Carlsten, 2019). Since 2013, surface O<sub>3</sub> concentration has increased  
35 over most parts of China, which is largely attributed to changes in anthropogenic emissions (Xu et al. 2018).  
36 However, previous studies have shown that in addition to its trend of change, surface O<sub>3</sub> concentration also  
37 demonstrated large interannual variations with significant regional differences (Zhou et al. 2013; Chen et al. 2019).  
38 Based on analysis of 11 years of observational data over Hong Kong, Zhou et al. (2013) reported that the  
39 interannual variation of O<sub>3</sub> concentration observed during 2000–2010 could reach up to 30% of the annual average  
40 concentration. The O<sub>3</sub> concentration in Beijing also showed evident interannual variation during 2006–2016. For  
41 example, the O<sub>3</sub> concentrations in the summers of 2012–2013 were lower by about 10 ppbv than that in 2011 and  
42 2014 (Chen et al. 2019).

43 High O<sub>3</sub> events are usually associated with meteorological factors (e.g., intense solar radiation, high air  
44 temperature and low humidity) favorable for O<sub>3</sub> formation, which can accelerate photochemical reaction and  
45 weaken the dispersions and depositions (Han et al. 2020). For example, Lu et al. (2019) designed sensitivity  
46 simulations to confirm that ozone pollution in China in 2017 was more serious than that in 2016, which was  
47 attributed to the large enhancement of nature emissions of ozone precursors caused by hot and dry climate  
48 condition in 2017. In the summer of 2013, the Yangtze River Delta experienced a severe heat wave with more  
49 stagnant meteorological conditions. The upper-level anticyclonic circulation with sink airflows led to abnormally  
50 low atmospheric water vapor content above the Yangtze River Delta and thus less than normal cloud cover, which  
51 was conducive to a strong solar radiation environment and significant increases in surface ozone (Pu et al. 2017).  
52 On the interannual to decadal time scale, anticyclonic anomalies over North China (NC) were critical for O<sub>3</sub>  
53 distribution in the summer and remotely linked with the effects of Eurasia teleconnection (EU) and west Pacific  
54 patterns (Yin et al. 2019).

55 The Arctic sea ice (SI) declined rapidly while its variability has been increasing over the past decades, which  
56 significantly affected summer atmospheric circulations over Eurasia (Lin and Li 2018). The preceding Arctic SI  
57 anomalies could aggravate anomalously high air temperature and drought disasters in NC by triggering EU-like  
58 atmospheric responses in summer (Wang and He 2015). Spring SI anomalies in the Barents Sea could prompt the  
59 Silk Road Pattern and resulted in a north-south dipole pattern of summer air temperature anomalies in the east of  
60 China (Li et al. 2021). When greater than normal SI occurred in the Barents Sea, local 500 hPa geopotential height  
61 would decrease and a wave-chain would form, which subsequently induced more precipitation in the south of East

62 China but less precipitation in the north (Wang and Guo 2004). Sea surface temperature (SST) in the Pacific and  
63 Indian oceans also have significant effects on atmospheric circulation over the east of China (Li and Xiao 2021;  
64 Xia et al. 2021). SST anomalies in the South China Sea and the equatorial Eastern Indian Ocean could trigger the  
65 East Asian - Pacific pattern and resulted in a dipole pattern of summer temperature and precipitation in the east  
66 of China, i.e., areas to the north of the Yangtze River became cold and wet, while areas to the south were hot and  
67 dry (Han and Zhang 2009; Li et al. 2018). Tian and Fan (2019) found that winter SST in the southern Indian  
68 Ocean might affect spring-summer SST anomalies near Australia. In summer, the anomalous Hadley circulation  
69 in the western North Pacific played an important role in summer precipitation over the middle and lower reaches  
70 of the Yangtze River.

71 Although great attention in previous studies has been paid to the increase of ozone pollution, little is known  
72 about changes in the spatial pattern of summer-mean  $O_3$  in the east of China. As revealed by Yin and Ma (2020),  
73 the dominant pattern of daily-varying ozone pollution in the east of China showed an interannual variation that  
74 was mainly driven by the large-scale western Pacific subtropical high and the East Asian deep trough. For example,  
75 the frequent movements of the western Pacific subtropical high and the East Asian deep trough both contributed  
76 to the out-of-phase variations in  $O_3$  over North China and the Yangtze River Delta (Zhao and Wang 2017; Yin  
77 and Ma 2020). However, to the best of our knowledge, whether the north-south dipole pattern of the summer mean  
78  $O_3$  pollution existed in the east of China still remains unclear. In this study, we attempted to explore the dominant  
79 pattern of summertime  $O_3$  in the east of China and associated physical mechanisms behind. Its connections with  
80 preceding climate variability were also examined. The remainder of this paper was organized as follows. The data  
81 and methods are described in Section 2. Section 3 examined the dipole pattern of summertime  $O_3$  in the east of  
82 China and its possible influencing factors. The associated physical mechanisms were studied in Section 4. Major  
83 conclusions and discussion are provided in Section 5.

## 84 **2. Datasets and methods**

### 85 **2.1 Observations and Reanalysis Dataset**

86 Hourly ozone concentration observations from 2015 to 2019 were publicly available at  
87 <https://quotsoft.net/air/> and the last accessible data were for 23 September 2020. The relevant data were detrended  
88 before all computations were conducted for the study period.

89 The meteorological fields data with a horizontal resolution of  $0.5^\circ$  latitude by  $0.625^\circ$  longitude for the period  
90 1980–2019 were taken from the MERRA-2 dataset (Gelaro et al., 2017), including geopotential height at 500 hPa

91 (Z500), surface incoming shortwave flux (Ssr), low and medium cloud cover (Mlcc), precipitation (Prec), 10-m  
 92 zonal and meridional winds (UV10m), and surface air temperature (SAT) and zonal and meridional winds and  
 93 vertical velocity at different vertical levels. Monthly OLR data ( $1^\circ \times 1^\circ$ ) could be acquired from the University of  
 94 Maryland OLR Climate Data Record portal (<http://olr.umd.edu/>). Monthly SI concentrations and SST ( $1^\circ \times 1^\circ$ )  
 95 for the period 1980 - 2019 were downloaded from the website of the Met Office Hadley Centre (Rayner et al.  
 96 2003). Monthly mean subsurface ocean temperatures in the upper 250 m with a horizontal resolution of  $1^\circ \times 1^\circ$   
 97 were obtained from the Met Office Hadley Centre EN4 version 2.1 (Good et al. 2013).

98 The wave activity flux (WAF) was computed to illustrate the propagation of Rossby wave activities (Takaya  
 99 and Nakamura 2001):

$$100 \quad W = \frac{1}{2|\bar{U}|} \left[ \bar{u}(\psi'^2_x - \psi'\psi'_{xx}) + \bar{v}(\psi'_x\psi'_y - \psi'\psi'_{xy}) \right] \\ \left[ \bar{u}(\psi'_x\psi'_y - \psi'\psi'_{xy}) + \bar{v}(\psi'^2_y - \psi'\psi'_{yy}) \right]$$

101 where subscripts denote partial derivatives; the overbar and prime represent the climatological mean and  
 102 anomaly, respectively;  $\psi'$  represents the stream function anomaly.  $U$  is the horizontal wind speed;  $u$  and  $v$  are the  
 103 zonal and meridional wind components, respectively; and  $W$  denotes the two-dimensional Rossby WAF. The  
 104 Rossby wave source  $-\nabla \cdot V_x(f + \xi)$  proposed by Sardeshmukh and Hoskins (1988) is also calculated in this  
 105 study.  $V$ ,  $\xi$  and  $f$  refer to the horizontal wind velocity, relative vorticity and geostrophic parameter,  
 106 respectively.  $\nabla$  is horizontal gradient; subscript  $\chi$  represents divergent component.

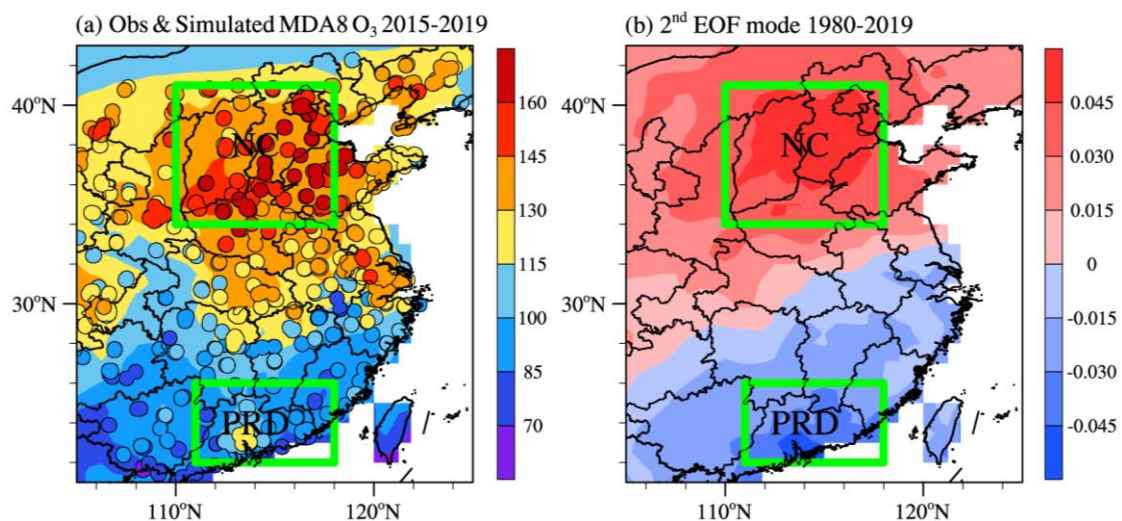
## 107 2.2 1980–2019 O<sub>3</sub> concentrations simulated by GEOS-Chem

108 Hourly ozone concentrations were simulated by the nested-grid version of the global 3-D chemical transport  
 109 model (GEOS-Chem), which included detailed description of oxidant–aerosol chemistry. The model was driven  
 110 by MERRA-2 assimilated meteorological data (Gelaro et al. 2017). The nested grid over China ( $15\text{--}55^\circ\text{N}$ ,  $75\text{--}$   
 111  $135^\circ\text{E}$ ) had a horizontal resolution of  $0.5^\circ$  latitude by  $0.625^\circ$  longitude and consisted of 47 vertical layers up to  
 112 0.01 hPa. The GEOS-Chem model included the fully coupled O<sub>3</sub>–NO<sub>x</sub>–hydrocarbon and aerosol chemistry  
 113 modules with more than 80 species and 300 reactions (Bey et al. 2001).

114 Chemical and physical processes were examined using the outputs of GEOS-Chem. Because non-local  
 115 planetary boundary layer (PBL) mixing was used, emissions and dry deposition trends within the PBL were  
 116 applied within the mixing (Holtslag and Boville, 1993). Compared with other terms, the value of wet deposition  
 117 was extremely small, so it was not considered in this study (Liao et al., 2006). Consequently, the major chemical  
 118 and physical processes related to meteorological conditions included the chemistry, convection, PBL mixing,  
 119 transport and their sum within the PBL were the focus.

120 The GEOS-Chem model has been widely used to examine historical O<sub>3</sub> changes in China. Yang et al. (2014)  
121 evaluated the simulated interannual variation of June–July–August (JJA) surface-layer O<sub>3</sub> concentration at the  
122 Hok Tsui station (22°13'N, 114°15'E). They found that the model could well capture the peaks and troughs of the  
123 observed JJA O<sub>3</sub> concentration with a high correlation coefficient of +0.87 (exceed the 99% confidence level)  
124 between simulations and observations. Moreover, the model could also realistically simulate the spatial  
125 distribution of O<sub>3</sub>, and the spatial correlation coefficient between simulations and observations in the summer of  
126 2017 could reach up to 0.89 (Li et al. 2019). These studies indicated that the GEOS-Chem model could capture  
127 the interannual variation and distribution of the surface O<sub>3</sub> concentration fairly well.

128 The GEOS-Chem model successfully reproduced the dominant patterns of summer O<sub>3</sub> pollution on a daily  
129 scale from 2015 to 2019 (Yin and Ma 2020). In this study, we first simulated the maximum daily average 8 h  
130 concentration of O<sub>3</sub> (MDA8 O<sub>3</sub>) from 2015 to 2019 and evaluated the performance of GEOS-Chem. The simulated  
131 spatial distribution of MDA8 O<sub>3</sub> was similar to that of observations with a spatial correlation coefficient of 0.87  
132 (Figure 1a). Compared the simulated and observed summer mean MDA8 O<sub>3</sub> concentrations in NC and the PRD,  
133 which had a low bias with a mean absolute error of 5.7 μg m<sup>-3</sup> and 12.1 μg m<sup>-3</sup> in the PRD and NC, respectively.  
134 The values of root mean square error / mean were 15.8 % and 8.1 % in NC and the PRD, respectively. The observed  
135 and simulated summer MDA8 O<sub>3</sub> anomalies in the east of China also presented consistent interannual differences  
136 (Figure S1 a, b). The high consistency in both the temporal and spatial distributions between the simulations and  
137 observations provided a solid evidence to support the feasibility of the present study.



138  
139 **Figure 1.** (a) Spatial distributions of observed (dots) and GEOS-Chem simulated (shading) summer-mean MDA8 O<sub>3</sub> (unit: μg  
140 m<sup>-3</sup>) for the period 2015–2019. (b) The second EOF spatial pattern of simulated summer-mean MDA8 O<sub>3</sub> from 1980 to 2019.  
141 The simulated O<sub>3</sub> concentrations were produced by GEOS-Chem with fixed emissions but changing meteorological conditions  
142 from 1980 to 2019. The green boxes represent the areas of NC and the PRD.

143 Based the above results, the GEOS-Chem model was then driven by fixed anthropogenic and natural  
144 emissions in 2010 and changing meteorological fields from 1980 to 2019 to highlight the impact of climate  
145 variability on O<sub>3</sub> concentration. Results of this simulation were analyzed to reveal the dominant pattern of ozone  
146 pollution in the east of China in summer and its relationship with preceding climate anomalies.

### 147 **2.3 Numerical experiments with CESM-LE**

148 To provide evidences that support the proposed connections between SI and SST and large-scale atmospheric  
149 circulations, the simulations of the Community Earth System Model Large Ensemble (CESM-LE) were employed  
150 (Kay et al. 2015). The CESM consists of coupled atmosphere, ocean, land, and sea ice component models. The  
151 40-member ensemble of CESM-LE simulations over the period (1980–2019) includes a historical simulation  
152 (1980–2005) and a representative concentration pathway (RCP) 8.5 forcing simulation (2006–2019). To confirm  
153 the impact of preceding climate variability and associated physical mechanisms, composite analyses were  
154 conducted based on the three years with the lowest and highest simulated preceding climatic variability for a  
155 particular month in each member. The composite results of atmospheric circulations could be considered as the  
156 relevant atmospheric responses associated with the preceding climate variability.

### 157 **3. Dipole pattern of summer O<sub>3</sub> and possible influencing factors**

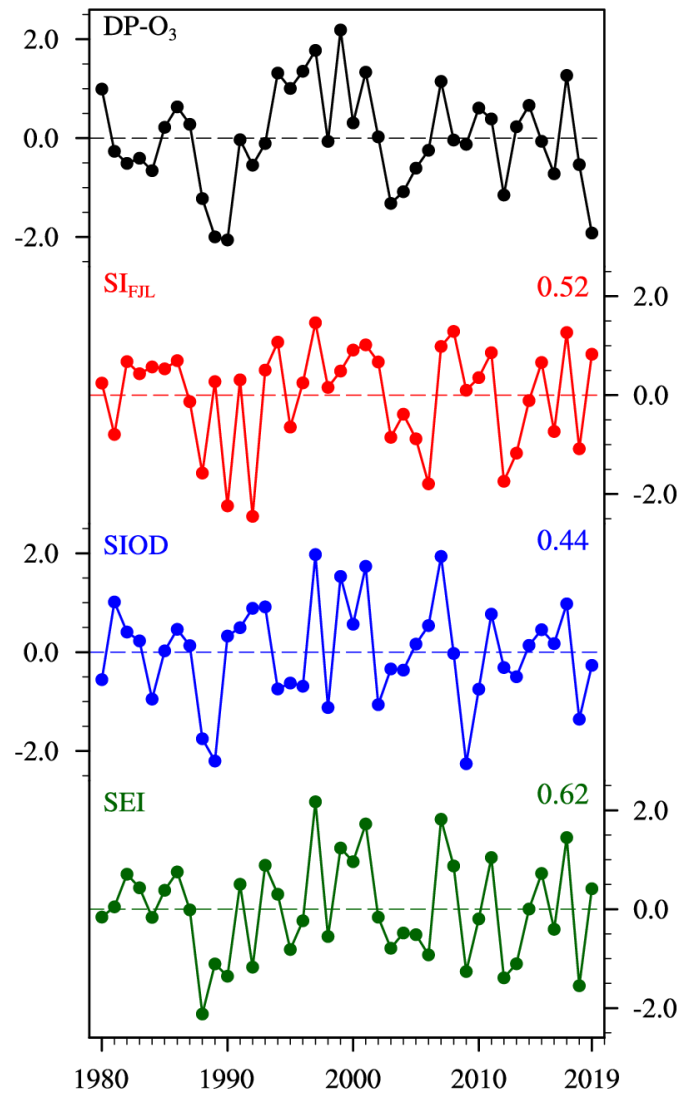
158 As aforementioned, the GEOS-Chem model has a good performance in simulating O<sub>3</sub> concentration. The  
159 summer O<sub>3</sub> concentrations from 1980 to 2019 was simulated by GEOS-Chem, and the EOF approach was applied  
160 to the GEOS-Chem simulation to explore the dominant patterns of summer mean O<sub>3</sub> pollution in the east of China.  
161 Percentage contributions to the total variance by the first and second EOF modes were 39% and 17.5%,  
162 respectively. The significance test of the EOF eigenvalues confirmed that the first and second patterns were  
163 distinctly separated (passing the North test, North et al, 1982). The first EOF pattern displayed a monopole pattern  
164 (Figure S2). The second EOF pattern presented a north-south dipole pattern of O<sub>3</sub> (DP-O<sub>3</sub>) distribution in the east  
165 of China with the two centers located in NC and the Pearl River Delta (PRD, Figure 1b), respectively. Observations  
166 have shown that high O<sub>3</sub> concentration frequently occurs in NC, and O<sub>3</sub> pollution in the PRD has become  
167 increasingly serious in recent years (Liu et al. 2020). Furthermore, about 80% of the MDA8 O<sub>3</sub> anomalies in NC  
168 were in opposite sign to those in PRD during 2015–2019 (Figure S1a, b). Therefore, despite the fact that it was  
169 only the second leading EOF mode, we still focused on the investigation of DP-O<sub>3</sub> in the present study, since it  
170 was more similar to the actual pollution situation. Impacts of climate variability are also analyzed.

171 The MDA8 O<sub>3</sub> anomalies were divided into positive (P) and negative phases (N) of DP-O<sub>3</sub> (Figure S3). For  
172 convenience, DP-O<sub>3</sub>P and DP-O<sub>3</sub>N were defined by the EOF time series of DP-O<sub>3</sub> greater than 1 standard

173 deviation and less than  $-1 \times$  standard deviation, respectively. The DP-O<sub>3</sub>P corresponded to positive anomalies of  
174 MDA8 O<sub>3</sub> in the north and negative anomalies in the PRD (Figure S3a). In contrast, high concentration of O<sub>3</sub>  
175 occurred in the PRD and low concentration center appeared in NC under the DP-O<sub>3</sub>N condition (Figure S3b). The  
176 correlation coefficient between time series of DP-O<sub>3</sub> and MDA8 O<sub>3</sub> difference between NC and the PRD was 0.91,  
177 indicating that DP-O<sub>3</sub> reflected the opposite changes of O<sub>3</sub> concentration in NC and the PRD.

178 With fixed emissions, the changes in O<sub>3</sub> concentrations from 1980 to 2019 were solely caused by  
179 meteorological conditions. The time series of DP-O<sub>3</sub> showed a strong interannual variation (Figure 2). Composite  
180 differences in large-scale atmospheric circulation and meteorological condition related to DP-O<sub>3</sub> between the  
181 positive and negative phases (DP-O<sub>3</sub>P minus DP-O<sub>3</sub>N) were analyzed to explore the impacts of atmospheric  
182 circulation on photochemical reactions and accumulations of various pollutants in the above two areas. During  
183 the positive phase of DP-O<sub>3</sub>, cyclonic and anticyclonic anomalies in the middle troposphere were found over the  
184 PRD and NC ( $C_{\text{PRD}}$  and  $AC_{\text{NC}}$ ) (Figure 3a), respectively. The  $C_{\text{PRD}}$  accompanied southerly winds in the PRD  
185 efficiently transported clean and moist air from the sea to the PRD (Figure 3c). Furthermore, low and medium  
186 cloud covers were significantly increased, which led to weak solar radiation and reduced photochemical reactions  
187 (Figure 3b). A moist, cool environment and weak solar radiation were conducive to low O<sub>3</sub> concentration in the  
188 PRD. On the other hand, the positive anomalies of geopotential height in NC increased surface air temperature  
189 (Figure 3a), resulting in a dry environment with decreased cloud covers and sunny weather (Figure 3b, c).

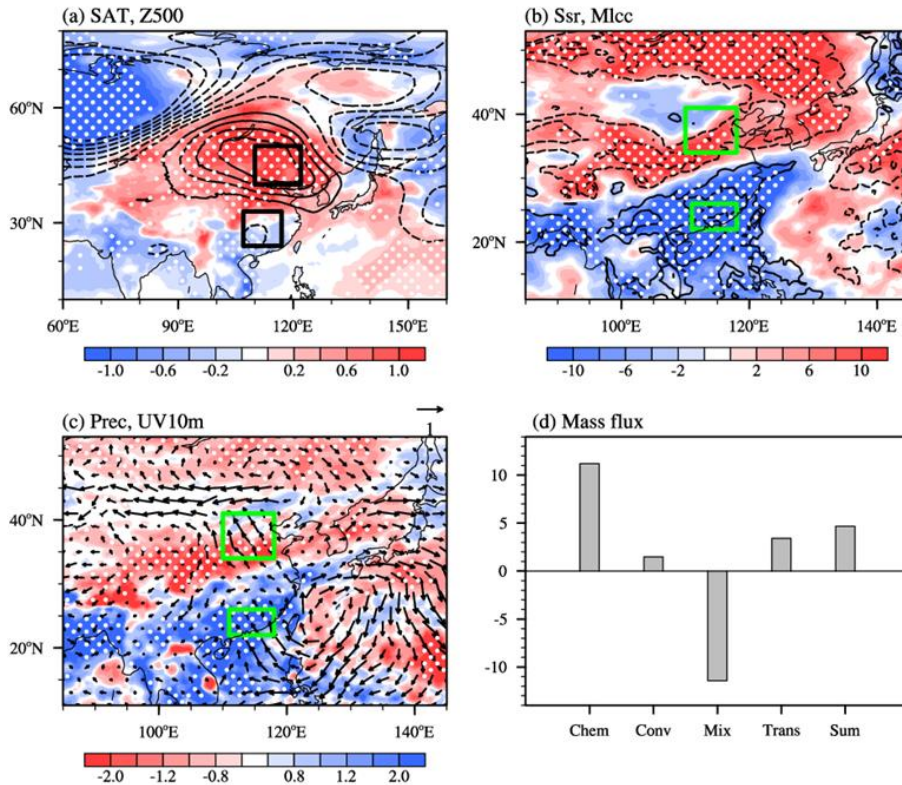
190 In order to provide a more quantitative evaluation of the contribution of chemical and physical processes, in  
191 Figure 3d, we examine the area-averaged differences in O<sub>3</sub> changes for NC and PRD. Chemistry represents the  
192 changes in net chemical production, which appears to be the dominating process, leading to the greatest O<sub>3</sub> change  
193 between NC and the PRD (12.3 Tons d<sup>-1</sup>, Figure 3d). Transport represents the change in horizontal and vertical  
194 advection of ozone. Depending on the ozone concentration gradient and wind anomalies, the transport difference  
195 between NC and PRD is 3.1 Tons d<sup>-1</sup> (Figure 3d). Convection changes slightly in NC and PRD. As the mixing  
196 process transports ozone along the vertical concentration gradient, it generally contributes negatively to the total  
197 ozone change. The above analysis indicates that different meteorological conditions between NC and the PRD led  
198 to the difference of O<sub>3</sub> concentration in the two regions (differed by 5.2 Tons d<sup>-1</sup>), which eventually contributed  
199 the formation of DP-O<sub>3</sub>.



200

201 **Figure 2.** Variations in standardized DP-O<sub>3</sub> time series (black), May SI near the Franz Josef Land (SI<sub>FJL</sub>, red), January–  
 202 February–March mean Subtropical Indian Ocean Dipole (SIOD, blue), and SEI (green) from 1980 to 2019. SEI defined as the  
 203 weighted average of SI<sub>FJL</sub> and SIOD. The correlation coefficients of the DP-O<sub>3</sub> with SI<sub>FJL</sub> (red), SIOD (blue), and SEI (green)  
 204 were shown in the figure.



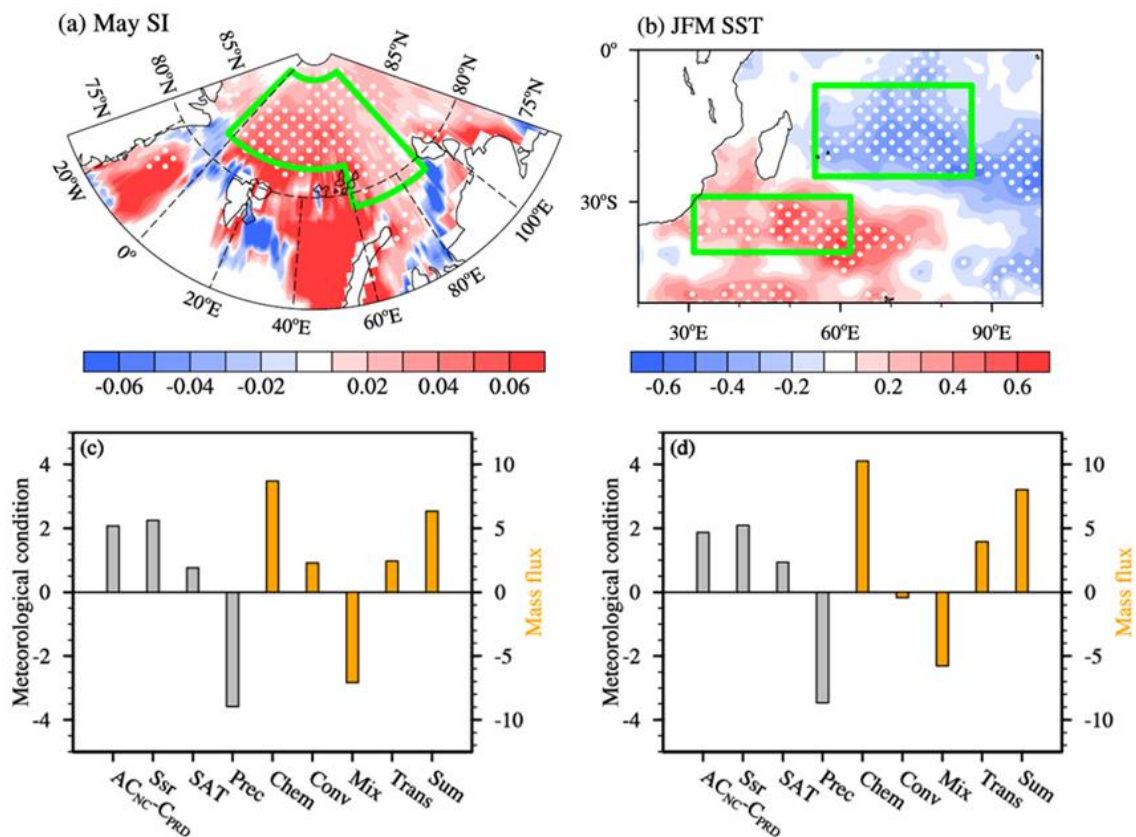


205

206 **Figure 3.** Composite summer atmospheric circulations associated with the DP-O<sub>3</sub> (DP-O<sub>3</sub>P minus DP-O<sub>3</sub>N) for the period  
 207 1980 to 2019, including (a) surface air temperature (SAT, unit: K, shadings) and geopotential height at 500 hPa (unit: 10 gpm,  
 208 contours), (b) surface incoming shortwave flux (Ssr, unit: W m<sup>-2</sup>, shadings) and low and medium cloud cover (Mlcc, unit: 1,  
 209 contours), and (c) precipitation (Prec, unit: mm, shadings) and surface wind (unit: m s<sup>-1</sup>, arrows). The white dots indicate that  
 210 the composites with shading were above the 90% confidence level. The black boxes in (a) indicate the centers of the AC<sub>NC</sub> and  
 211 C<sub>PRD</sub>, respectively. The green boxes in (b) and (c) represent the areas of NC and the PRD. Composites of the summer mass  
 212 fluxes of O<sub>3</sub> (d) associated with the DP-O<sub>3</sub> (DP-O<sub>3</sub>P minus DP-O<sub>3</sub>N) for the area-averaged differences (NC minus PRD) from  
 213 1980 to 2019. The bottom axis gives the names of the chemical and physical processes: chemical reaction (Chem), convection  
 214 (Conv), PBL mixing (Mix), transport (Trans) and their sum (Sum).

215 Arctic SI in May was closely related to summer O<sub>3</sub> pollution in NC (Yin et al. 2019), but its effects on the  
 216 north-south dipole distribution of O<sub>3</sub> had not been studied. The meridional O<sub>3</sub> dipole pattern in the east of China  
 217 was positively correlated with SI anomalies near the Franz Josef Land (SI<sub>FJL</sub>). Note that the correlation between  
 218 them remains unchanged after the signal of El Niño-Southern Oscillation (ENSO) was removed. The area-  
 219 averaged (82–88°N, 3°W–60°E; 79–88°N, 60–90°E; denoted by the green boxes in Figure 4a) SI in May was  
 220 calculated and defined as the SI<sub>FJL</sub> index, whose linear correlation coefficient with the time series of DP-O<sub>3</sub> was  
 221 0.52 (exceeding the 99% confidence level). When the SI<sub>FJL</sub> anomalies were significant (i.e., |anomalies| > its one  
 222 standard deviation), the occurrence probability of the DP-O<sub>3</sub> in the same phase was 83% (Figure 2). Furthermore,  
 223 the active centers of the anomalous atmospheric circulations and meteorological conditions associated with SI<sub>FJL</sub>  
 224 in the east of China were similar to that of the DP-O<sub>3</sub> (i.e., NC and PRD). That is, positive SI<sub>FJL</sub> anomalies were  
 225 conducive to less (more) precipitation, less (more) cloud cover, and strong (weak) solar radiation in NC (PRD)

226 (Figure 4c, Figure S4). The chemical and physical processes of ozone production in GEOS-Chem simulations  
 227 were analyzed. The difference of chemical reactions between NC and PRD had a large positive value (11.6 Tons  
 228  $\text{d}^{-1}$ ), and the difference of the sum of all chemical and physical processes was 7.0 Tons  $\text{d}^{-1}$  (Figure 4c), resulting  
 229 in DP- $\text{O}_3$ .



230  
 231 **Figure 4.** Composites of (a) May SI concentration and (b) JFM SST associated with the DP- $\text{O}_3$  (DP- $\text{O}_3\text{P}$  minus DP- $\text{O}_3\text{N}$ ) from  
 232 1980 to 2019. The green boxes in (a) and (b) indicate where the  $\text{SI}_{\text{FJL}}$  and SIOD indices are calculated, respectively. The white  
 233 dots indicate that the composites were above the 90% confidence level. Composite summer meteorological conditions,  
 234 circulations and mass fluxes of  $\text{O}_3$  associated with (c)  $\text{SI}_{\text{FJL}}$  (positive  $\text{SI}_{\text{FJL}}$  years minus negative  $\text{SI}_{\text{FJL}}$  years) and (d) SIOD  
 235 (positive SIOD years minus negative SIOD years) from 1980 to 2019. The bottom axis gives the names of the meteorological  
 236 conditions and chemical and physical processes: the differences between  $\text{AC}_{\text{NC}}$  and  $\text{C}_{\text{PRD}}$  (unit: 10 gpm), surface incoming  
 237 shortwave flux (Ssr, unit:  $\text{W m}^{-2}$ ), surface air temperature (SAT, unit: K), and precipitation (Prec, unit: mm); chemical reaction  
 238 (Chem, unit: Tons  $\text{d}^{-1}$ ), convection (Conv, unit: Tons  $\text{d}^{-1}$ ), PBL mixing (Mix, unit: Tons  $\text{d}^{-1}$ ), transport (Trans, unit: Tons  $\text{d}^{-1}$ )  
 239 and their sum (Sum, unit: Tons  $\text{d}^{-1}$ ).

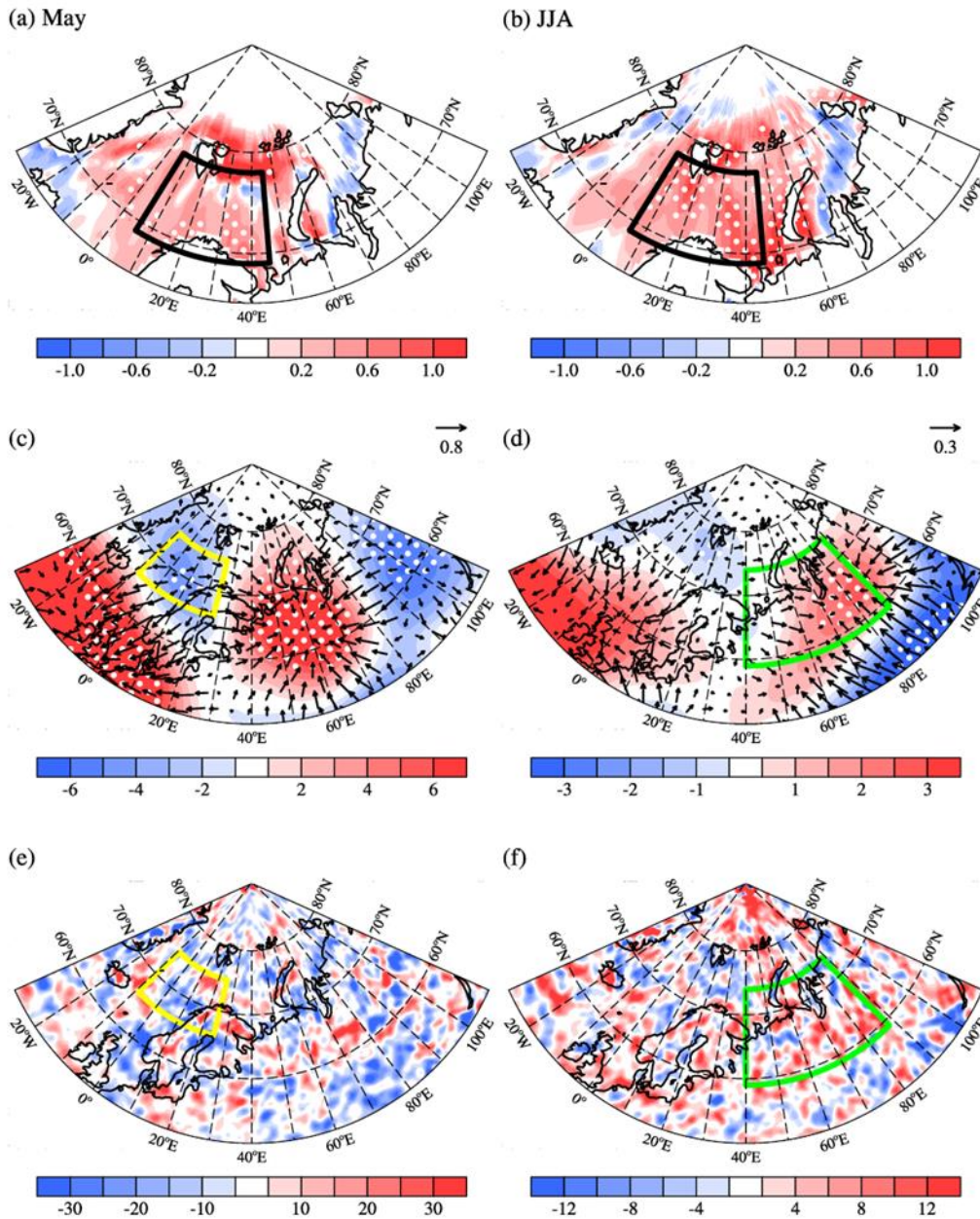
240 In addition to the signal from the Arctic, SST as an effective external forcing also has significant influences  
 241 on summer climate in the east of China (Li et al. 2018). Therefore, it was important to answer the question whether  
 242 SST could affect the DP- $\text{O}_3$  in the east of China in summer. Large anomalies of preceding January–February–  
 243 March (JFM) SST over the southern Indian Ocean was obvious when we evaluated the relationship between the  
 244 DP- $\text{O}_3$  and previous SST. After removing the influence of ENSO, the SST signal in the southern Indian Ocean  
 245 still maintains (Figure 4b). The two regions with significant anomalies were similar to the Subtropical Indian

246 Ocean Dipole (SIOD) regions found by Behera and Yamagata (2001). Variance analysis and correlation analysis  
247 of SST in the Indian Ocean also indicated that a SST dipole type oscillation occurred in the southern Indian Ocean,  
248 which usually developed in the preceding winter and reaches its strongest in the subsequent January to March (Jia  
249 and Li 2013). The difference between the mean SST of the two regions (29–40°S, 31–62°E and 7–25°S, 55–86°E;  
250 green box in Figure 4b; the southwest positive pole minus the northeast negative pole) was defined as the SIOD  
251 index and calculated (Figure 2). The linear correlation coefficient between the SIOD index and the time series of  
252 DP-O<sub>3</sub> from 1980 to 2019 was 0.44 (significant at the 99% confidence level). When the SIOD anomalies were  
253 significant (i.e., |anomalies| > its one standard deviation), the occurrence probability of DP-O<sub>3</sub> in the same phase  
254 is 82% (Figure 2). Furthermore, the composite meteorological conditions in the positive and negative phases of  
255 SIOD had similar centers to that of DP-O<sub>3</sub>. That is, the anticyclone over NC was always accompanied by hot-dry  
256 meteorological condition, while the cyclone over PRD was always accompanied by cool-moist environment  
257 (Figure 4d; Figure S5). The chemical reactions increased 12.3 Tons d<sup>-1</sup> in NC comparing to those in the PRD  
258 (Figure 4 d), indicating that the strong solar radiation and high temperature conditions actually enhanced the  
259 chemical reactions in the atmosphere to produce more O<sub>3</sub> in NC.

#### 260 **4. Associated physical mechanisms**

261 Changes in SI<sub>FJL</sub> and SIOD both could possibly contribute to the formation of DP-O<sub>3</sub>. Note that SI<sub>FJL</sub> and  
262 SIOD have few years of common significant anomalies, more than 78% of the individual sample years were used  
263 to make composite with both indices. The correlation coefficient between them was only 0.21 and was not  
264 significant, indicating that SI<sub>FJL</sub> and SIOD were independent of each other. Several previous studies have  
265 documented that the preceding Arctic SI anomalies could trigger EU-like atmospheric responses in the subsequent  
266 summer, and thus influenced the climate in the east of China (Wang and He 2015). Corresponding to reduced  
267 SI<sub>FJL</sub>, SST anomalies in the Barents and Kara Sea were significantly positive and gradually increase from May to  
268 summer months (Figure 5a, b). The warm SST anomalies influenced local heat anomalies and caused anomalous  
269 atmospheric circulations. Following the decrease in SI<sub>FJL</sub>, anomalous divergent winds appeared in the mid-  
270 troposphere, which were accompanied by warm SST anomalies and negative velocity potential anomalies (yellow  
271 box in Figure 5c). As proposed by Xu et al., (2021), the rotational component of the anomalous divergent winds  
272 could spread to the south and force the vorticity generation over Eurasia. Thus, during the subsequent summer,  
273 significant convergence and positive velocity potential with a positive Rossby wave source anomaly occurred over  
274 northern Europe and West Siberia (green box in Figure 5d). We also used the SST anomalies associated with SI<sub>FJL</sub>  
275 (in Barents and Kara Sea in JJA) to composite relevant variables. Significant convergence, positive velocity

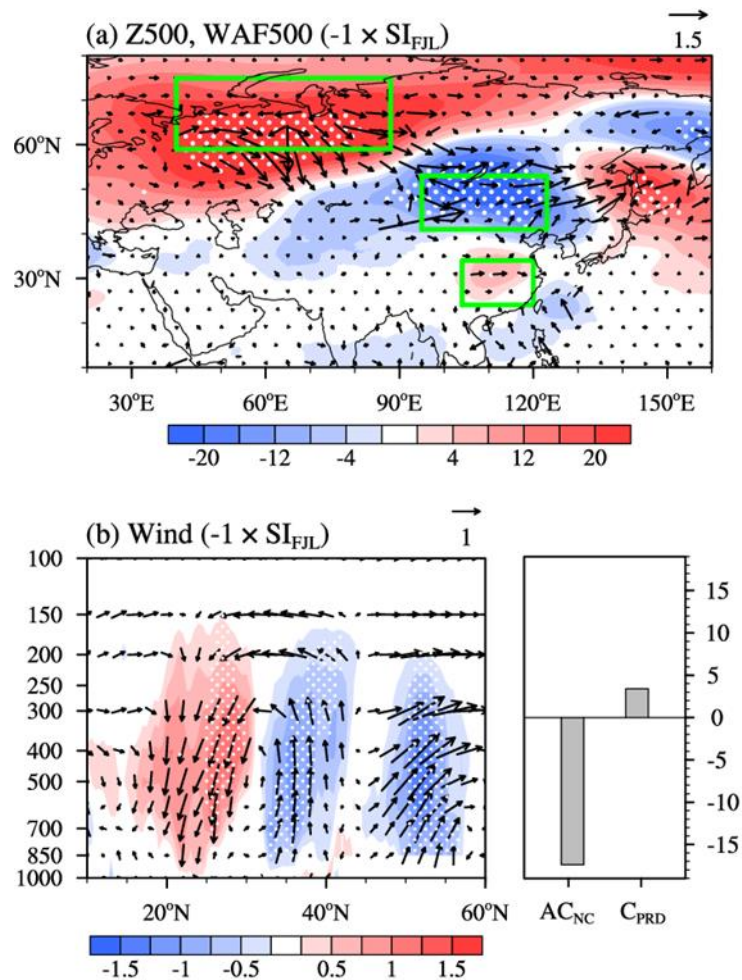
276 potential, and positive Rossby source anomaly all appeared over Europe and West Siberia in JJA (Figure S6). This  
 277 indicated that positive anomalies of Rossby-wave source over Europe and West Siberia could be generated  
 278 by local heat anomalies associated with decreased  $SI_{FJL}$  in the Barents and Kara Sea.



279  
 280 **Figure 5.** Composites of (a) May Arctic SST (unit: K), (c) velocity potential (unit:  $10^5 \text{ m}^2 \text{ s}^{-1}$ , shading) and divergent wind at  
 281 500 hPa (unit:  $\text{m s}^{-1}$ , arrows), and (e) Rossby wave source anomalies at 500 hPa (unit:  $10^{-11} \text{ s}^{-2}$ ) associated with  $SI_{FJL}$  index  
 282 (negative  $SI_{FJL}$  years minus positive  $SI_{FJL}$  years) from 1980 to 2019. The back box in (a) and (b), yellow box in (c) and (e) and  
 283 green box in (d) and (f) represents the center of the SST, velocity potential and Rossby wave source anomaly associated with  
 284  $SI_{FJL}$ , respectively. The white dots indicate that the composites with shading were above the 90% confidence level.

285 Moreover, corresponding to the decreased  $SI_{FJL}$ , the anomalous Rossby WAF propagated from Europe and  
 286 West Siberia (consistent with the aforementioned Rossby wave source) to Northeast China and enhanced the  
 287 cyclonic anomaly nearby (Figure 6a). The anomalous cyclonic circulation caused ascending motion from the

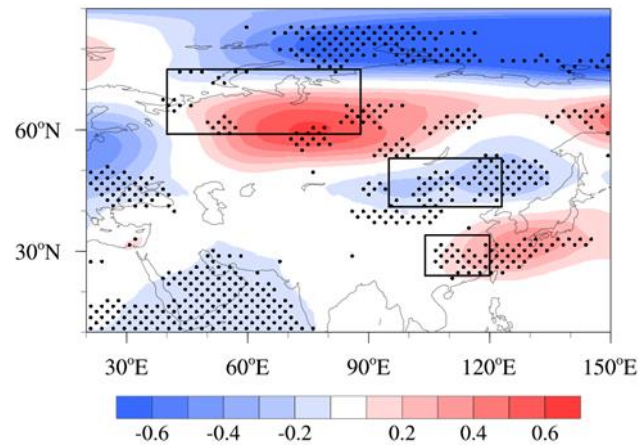
288 surface up to 300 hPa over NC, and further induced a meridional circulation with an anomalous descending branch  
 289 near 20°N (Figure 6b). Likewise, an anomalous anticyclone occurred in the middle troposphere above the PRD  
 290 (Figure 6b). In other words, an EU-like Rossby wave train was induced in the mid-troposphere (Figure 6a), which  
 291 propagated from northern Europe and West Siberian Plain (+), reaching the broad area from northeastern China  
 292 (-) to the south of China (+). Thus, the reduction in SI near the Franz Josef Land in the May modulated the EU-  
 293 like pattern in the subsequent summer and strengthened the anomalous cyclonic and anticyclonic circulations over  
 294 NC and the PRD (Figure 6b), respectively. The differences in anomalous atmospheric circulations and associated  
 295 meteorological conditions between NC and the PRD make great contributions to the occurrence of DP-O<sub>3</sub>.



296  
 297 **Figure 6.** Composites of (a) wave activity flux anomalies (unit:  $\text{m}^2 \text{s}^{-2}$ , arrows), geopotential height (unit: gpm, shading) at  
 298 500 hPa and (b) mean wind (unit:  $\text{m s}^{-1}$ , arrows), omega (unit:  $10^{-2} \text{ Pa s}^{-1}$ , shading) over 100–130° E, and the anomalies of  
 299 AC<sub>NC</sub> and C<sub>PRD</sub> (unit: gpm, bar) in summer associated with SI<sub>FJL</sub> index (negative SI<sub>FJL</sub> years minus positive SI<sub>FJL</sub> years) from  
 300 1980 to 2019. The green boxes in (a) represent the centers of the EU-like pattern. The white dots indicate that the composites  
 301 with shading were above the 90% confidence level.

302 The relationship between the preceding May SI anomalies and the JJA EU-like pattern was also confirmed  
 303 by large ensemble simulations of CESM during 1980–2019. According to the simulated sea ice fraction near the  
 304 Franz Josef Land, the three years with the lowest and highest SI in each member were selected to construct the

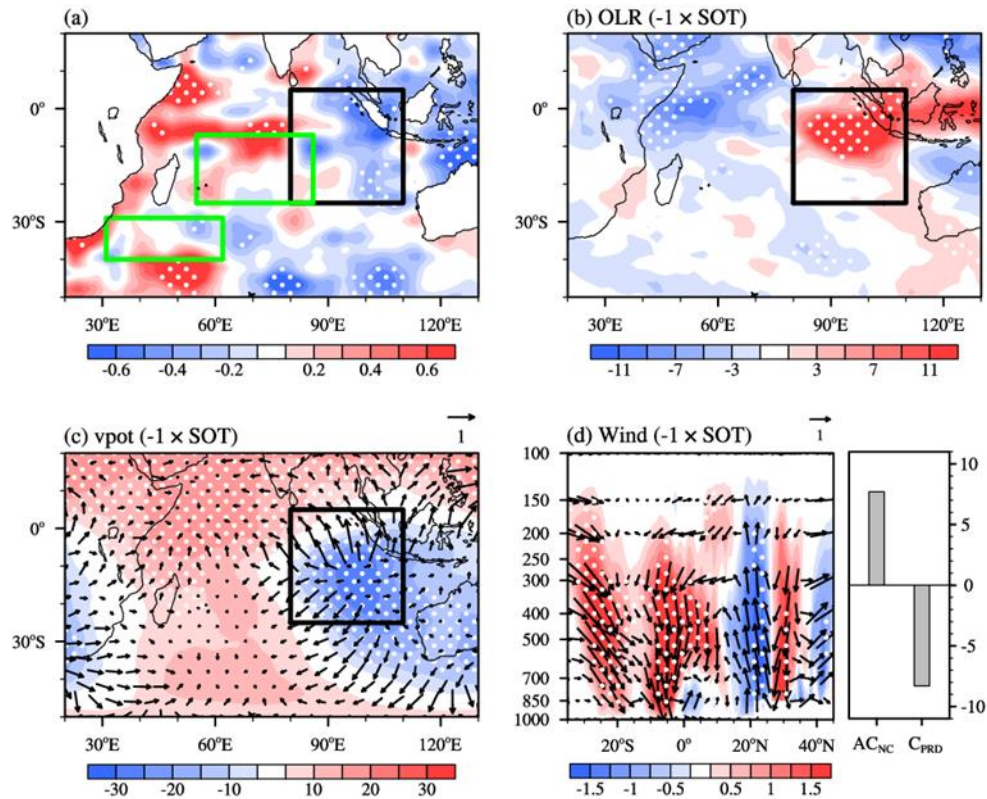
305 composite maps based on all the 40 available members. The difference in JJA geopotential height at 500 hPa  
 306 represented the atmospheric response to declining May  $SI_{FJL}$ . As shown in Figure 7, the decline of  $SI_{FJL}$  in May  
 307 led to an EU-like pattern in the subsequent summer over Eurasia, which was in good accordance with the observed  
 308 result (Figure 6a). The anticyclonic and cyclonic anomalies shown in the geopotential height at 500 hPa (i.e.,  
 309  $AC_{NC}$  and  $C_{PRD}$ ) in summer were also well reproduced by over 60% of the members. The above results confirmed  
 310 the robustness of the physical mechanisms proposed in the present study.



311  
 312 **Figure 7.** Composite differences of geopotential height at 500 hPa in JJA between three low and high  $SI_{FJL}$  years based on the  
 313 ensemble of 40 CESM-LE simulations during 1980–2019. The black dots indicate that the mathematical sign of the composite  
 314 results of more than 60 % of the members is consistent with the ensemble mean. The black boxes represent the centers of the  
 315 EU-like pattern.

316 SIOD could influence atmospheric anomalies and distribution of summer precipitation in China mainly  
 317 through Hadley circulation (Liu et al. 2019). Can SIOD anomalies also influenced the DP- $O_3$  via meridional  
 318 atmospheric forcing? Despite the significant correlation between SIOD anomalies (defined by SST) and the DP-  
 319  $O_3$  in the east of China (Figure 4b), it should be noted that the thermodynamic signals in the southern Indian Ocean  
 320 not only existed on the sea surface but also extended to the subsurface (Figure S7). As time goes by, the center of  
 321 negative SST anomalies moved to the northeast possibly due to the eastward movement of atmospheric forcing  
 322 caused by the mean westerly flow (Behera and Yamagata 2001). When it moved to the vicinity of Sumatra Island  
 323 in JJA, the abnormally cold signals of SST could extend downward from the surface to 60m (black box in Figure  
 324 8a). The area-averaged (black box in Figure 8a) summer-mean subsurface ocean temperature of 0–60m was  
 325 defined as the SOT index and calculated. Affected by negative SOT anomalies near Sumatra Island, the equatorial  
 326 eastern Indian Ocean convection was suppressed (indicated by positive anomalies of OLR in Figure 8b) and  
 327 significant divergence prevailed in the lower troposphere (Figure 8c). As a result, anomalous downward air flow  
 328 developed near Sumatra Island from 300 hPa to the surface (about 20–5°S in Figure 8d). This anomalous  
 329 downward air flow modulated the meridional circulation over 90–120 °E by strengthening the abnormal upward

330 airflow at 20°N and downward airflow at 30°N. Thus, the  $AC_{NC}$  and  $C_{PRD}$  were enhanced simultaneously (Figure  
 331 8d). Overall, following the positive phase of SIOD, the cold signal of SOT anomalies changed the meridional  
 332 circulation in the subsequent JJA and strengthened the  $C_{PRD}$  and  $AC_{NC}$  in the troposphere above the east of China.  
 333 Under these large-scale atmospheric anomalies,  $O_3$  concentrations became higher in NC, whereas the generation  
 334 of surface  $O_3$  were weakened in the PRD.

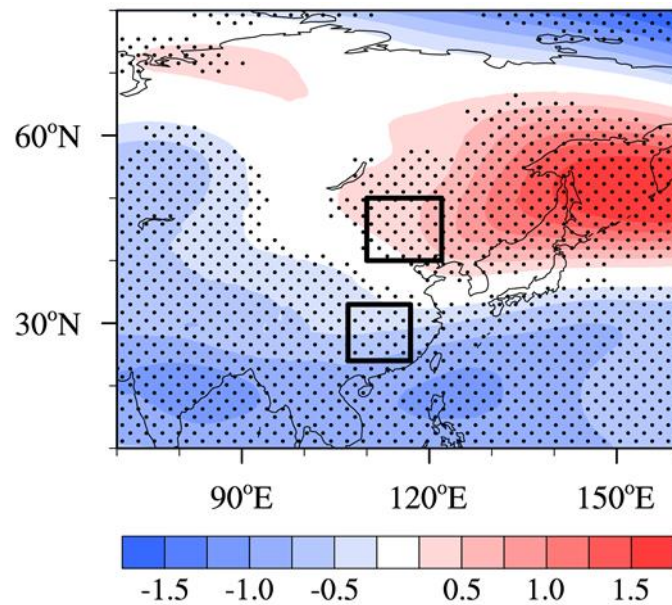


335

336 **Figure 8.** (a) Composites of mean 0–60m subsurface ocean temperature (unit: K) in summer associated with the SIOD  
 337 (positive SIOD years minus negative SIOD years) from 1980 to 2019. The green boxes represent the centers of the SIOD, and  
 338 the black box indicates where the SOT index is calculated. Composites of (b) OLR (unit:  $W m^{-2}$ ) and (c) velocity potential  
 339 (unit:  $10^5 m^2 s^{-1}$ , shadings) and divergent winds (unit:  $m s^{-1}$ , vectors) at 10 m in summer associated with SOT indexes of  
 340 opposite sign (negative SOT years minus positive SOT years). The black box represents the center of the SOT. (d) Composites  
 341 of summer mean winds (unit:  $m s^{-1}$ , arrows) and omega (unit:  $10^{-2} Pa s^{-1}$ , shadings) over 90–120°E, and the anomalies of  $AC_{NC}$   
 342 and  $C_{PRD}$  (unit: gpm, bars) associated with SOT indexes of opposite sign. The white dots indicate that the composites with  
 343 shading were above the 90% confidence level.

344 The CESM-LE datasets were also used to verify the statistical correlation between the preceding SIOD and  
 345 large-scale atmospheric circulations in JJA. The composite differences of SIOD in JFM between the three high  
 346 years and three low years of SST simulated by each ensemble member during 1980–2019 were investigated based  
 347 on the ensemble of 40 CESM-LE simulations. The composite results (positive SIOD years minus negative SIOD  
 348 years) of atmospheric circulations could be considered as the relevant atmospheric circulation responses  
 349 associated with differences in SIOD. More than 60% of the CESM ensemble members could well reproduce the

350 anticyclonic circulation over NC and the cyclonic circulation over the PRD in summer at 500hPa (Figure 9). That  
 351 is, the CESM-LE also confirmed the relationship between the previous JFM SIOD anomaly and the DP-O<sub>3</sub>-related  
 352 atmospheric circulations (i.e., AC<sub>NC</sub> and C<sub>PRD</sub>) in subsequent JJA.



353  
 354 **Figure 9.** Composite differences of geopotential height at 500 hPa in JJA between three high and low SIOD years based on  
 355 the ensemble of 40 CESM-LE simulations during 1980–2019. The black dots indicate that the mathematical sign of the  
 356 composite results of more than 60 % of the members is consistent with the ensemble mean. The black boxes represent the  
 357 centers of AC<sub>NC</sub> and C<sub>PRD</sub>, respectively.

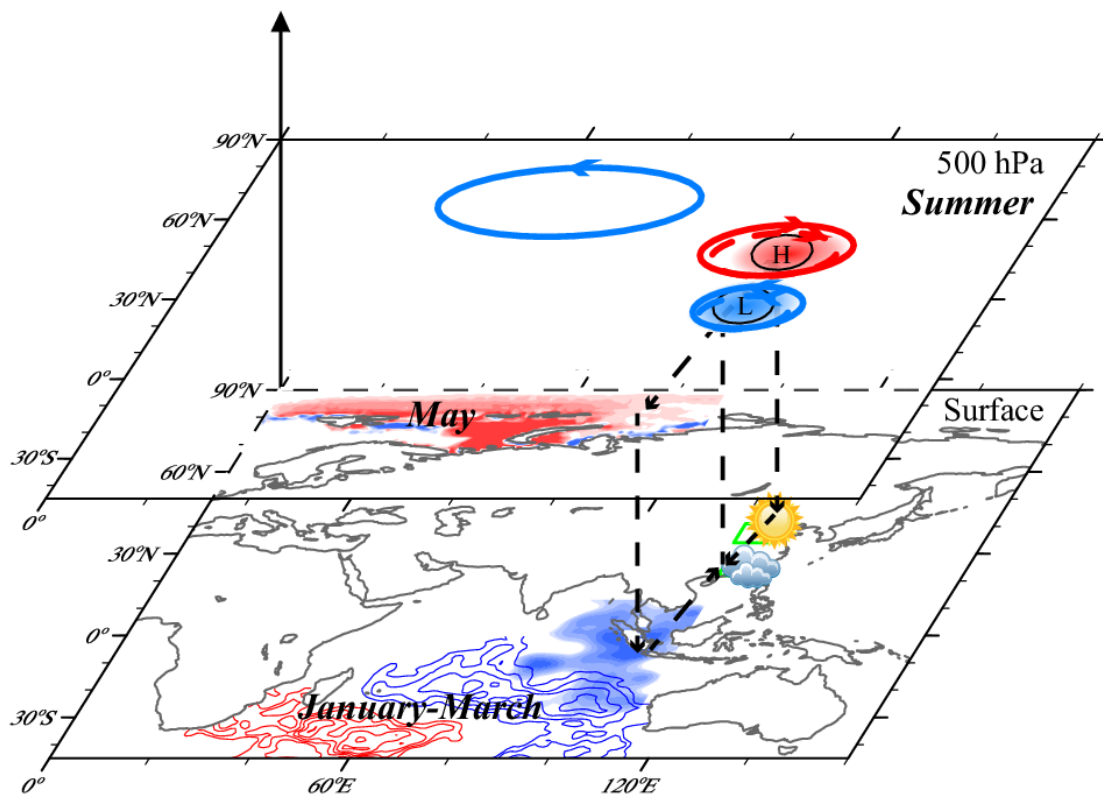
## 358 5. Conclusions and discussions

359 In general, the O<sub>3</sub> concentrations in NC were substantially high and the problem of O<sub>3</sub> pollution in the PRD  
 360 has become increasingly prominent in recent years. A south-north dipole pattern of O<sub>3</sub> concentration in the east of  
 361 China was identified based on GEOS-Chem simulations with fixed emissions and changing meteorological  
 362 condition from 1980 to 2019. The DP-O<sub>3</sub> pattern presented opposite centers in NC and PRD. Corresponding to  
 363 the positive phase of DP-O<sub>3</sub>, cyclonic and anticyclonic anomalies were located over the PRD and NC respectively,  
 364 which resulted in dry and hot climate in NC, while the environment in the PRD region was cool and moist. The  
 365 opposite was true in the negative phase of DP-O<sub>3</sub>. During positive phases, the meteorological condition mentioned  
 366 above significantly enhanced photochemical reactions in NC but suppressed O<sub>3</sub> production in the PRD, and thus  
 367 make great contributions to the south-north dipole pattern of O<sub>3</sub> in the east of China.

368 Arctic SI near the Franz Josef Land in May played an important role in the occurrence of DP-O<sub>3</sub>. The warm  
 369 SST anomalies associated with less SI<sub>FJL</sub> could induce divergent wind field and vorticity advection in the upper  
 370 layer, and enhanced positive Rossby wave source over northern Europe and West Siberia in summer. An EU-like



371 pattern was triggered in Eurasia (solid lines in Figure 10), which could enhance the DP-O<sub>3</sub>-related atmospheric  
 372 circulation (i.e., AC<sub>NC</sub> and C<sub>PRD</sub>) in JJA. As a result, meteorological conditions for O<sub>3</sub> concentration were  
 373 completely different between NC and PRD, which eventually contributed the formation of DP-O<sub>3</sub>. In addition, the  
 374 precursory climatic driving signal of SIOD anomalies in the low latitudes in JFM was also closely linked to DP-  
 375 O<sub>3</sub>. The thermodynamic signal of SIOD could be stored in the subsurface, and the center of negative SST  
 376 anomalies moved to the vicinity of Sumatra Island in summer. The meridional circulation intensified in summer  
 377 (dashed lines in Figure 10), which, along with the enhancement of the AC<sub>NC</sub> and C<sub>PRD</sub> over the east of China,  
 378 effectively increased O<sub>3</sub> concentration in NC but suppressed the generation of surface O<sub>3</sub> in the PRD. The linkages  
 379 and corresponding physical mechanisms were well reproduced by the large CESM-LE ensemble simulation.



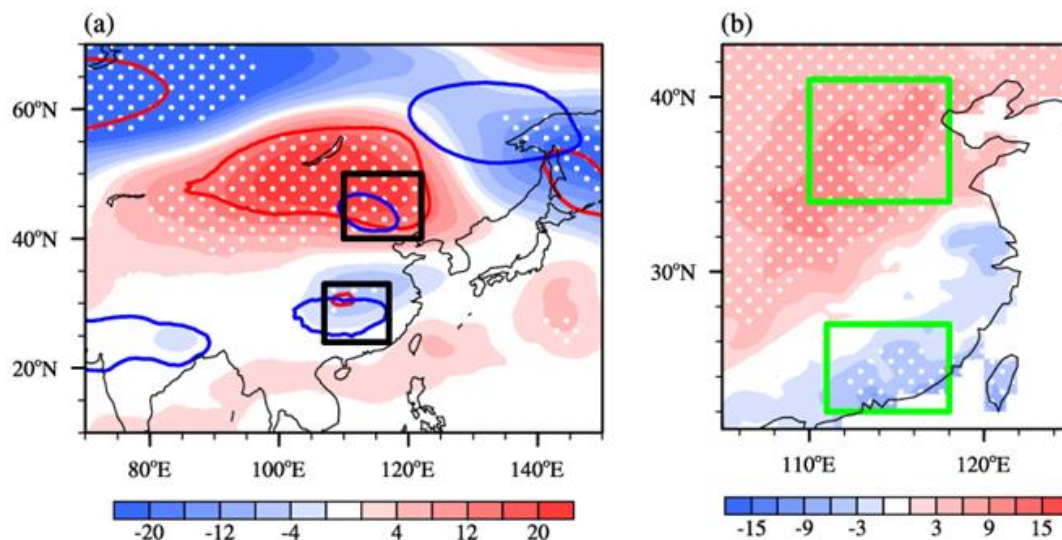
380  
 381 **Figure 10.** Schematic diagrams of the associated physical mechanisms. The May SI anomalies near the Franz Josef Land (red  
 382 shadings) could trigger an EU-like pattern in the atmosphere in summer, which enhances the anticyclonic anomaly over NC  
 383 and the cyclonic anomaly over the PRD. The thermodynamic signal of the preceding SIOD (contours) could be stored in the  
 384 subsurface and the center of negative SST anomalies moves to the vicinity of Sumatra Island in summer (blue shading). The  
 385 meridional circulation was enhanced in summer (dashed lines), along with the enhancement of AC<sub>NC</sub> and C<sub>PRD</sub> over eastern  
 386 China. The solid lines indicate the anomalous atmospheric circulations affected by SI<sub>FJL</sub>, while the dashed lines indicate the  
 387 anomalous atmospheric circulations affected by SIOD.

388 The above analysis has revealed that the DP-O<sub>3</sub> is independently affected by SIOD and SI<sub>FJL</sub> from 1980 to  
 389 2019. We attempted to discuss the combined impacts of the two precursory climatic drivers in the present  
 390 study. For this purpose, a synthetic climate variability index SEI, defined as the weighted average of SI<sub>FJL</sub> and

391 SIOD, is calculated by

$$392 \quad SEI = \frac{r_1 \times SI_{FJL} + r_2 \times SIOD}{|r_1| + |r_2|}$$

393 where  $r_1$  and  $r_2$  were the correlation coefficients of  $SI_{FJL}$  ( $r_1 = 0.52$ ) and SIOD ( $r_2 = 0.44$ ) with the DP- $O_3$   
394 time series, respectively. The correlation coefficient between SEI and DP- $O_3$  was 0.62 (Figure 2, exceeding the  
395 99% confidence level). When the SEI anomalies were significant, the occurrence probability of the DP- $O_3$  in the  
396 same phase was 93% (Figure 2), which is higher than that based on individual influences of the two factors.  
397 Composite atmospheric circulation analysis has been carried out based on years of positive and negative SEI  
398 anomalies, and the results are shown in Figure 11a. The composite atmospheric circulation based on the SEI index  
399 was stronger, resulting in the concentrations of MDA8  $O_3$  in NC was  $11.74 \mu\text{g m}^{-3}$  higher than that in PRD (Figure  
400 11b). The main areas influenced by SI and SST were slightly different. Although the two precursory climatic  
401 drivers both could affect the atmospheric circulations over NC and the PRD,  $SI_{FJL}$  mainly affected atmospheric  
402 circulation anomaly over NC, while SIOD played a major role in the PRD. However, climate variabilities at  
403 different latitudes jointly facilitated the dipole pattern of  $O_3$  in the east of China from 1980 to 2019.



404  
405 **Figure 11.** (a) Composites of geopotential height at 500 hPa (unit: gpm, shadings) in summer associated with the SEI (positive  
406 SEI years minus negative SEI years) from 1980 to 2019. The red and blue lines indicate areas where the composite  
407 geopotential height anomalies associated with  $SI_{FJL}$  and SIOD exceed the 90% confidence level, respectively. The black boxes  
408 represent the centers of AC<sub>NC</sub> and C<sub>PRD</sub>, respectively. (b) Composite differences of the detrended summer-mean MDA8  $O_3$   
409 (unit:  $\mu\text{g m}^{-3}$ ) simulated by GEOS-Chem model between high and low SEI years during 1980–2019. The white dots indicate  
410 that the composite differences are above the 90% confidence level. The green boxes represent the areas of NC and the PRD.

411 The north-south dipole pattern of  $O_3$  in the east of China in summer and its relationship with climate factors  
412 were clearly revealed in this study, yet some questions still remain unanswered and should be investigated in the  
413 future. The GEOS-Chem model simulations were used to explore the dominant pattern of  $O_3$  in the east of China

414 in summer due to the short sequence of O<sub>3</sub> observations. Although the GEOS-Chem demonstrated a good  
415 performance based on evaluation, there still exist some differences between the simulations and observations. In  
416 addition, statistical and numerical methods were used to reveal and verify the physical mechanisms behind the  
417 dipole pattern of O<sub>3</sub> in the east of China and its relation with climate variability. However, further numerical  
418 experiments should be carried out in the future. For example, coupled climate-chemistry models should be used  
419 to not only simulated the influence of climate driving factors on O<sub>3</sub> pattern, but also revealed the effect of  
420 individual climate factors as well as their comprehensive effects.

421

422

423 **Data Availability.** Hourly O<sub>3</sub> concentration data could be downloaded from <https://quotsoft.net/air/> (Ministry of  
424 Environmental Protection of China, the last accessible data are for 23 September 2020). Sea ice concentration,  
425 sea surface temperature, and subsurface ocean temperature data were from <https://www.metoffice.gov.uk/hadobs/>  
426 (Met Office Hadley Centre, 2020). Monthly-mean MERRA-2 reanalysis dataset was available at  
427 <https://disc.gsfc.nasa.gov/datasets?page=1> (MERRA-2, 2021). The monthly OLR data could be acquired from  
428 <http://olr.umd.edu/> (University of Maryland OLR Climate Data Record portal).

429

### 430 **Acknowledgements**

431 This work was supported by National Natural Science Foundation of China (42088101, 41991280, 42025502 and  
432 91744311).

433

### 434 **Authors' contribution**

435 Yin Z. C. designed the research. Ma X. Q. performed the research and analyzed the data. Yin Z. C. and Ma X. Q.  
436 prepared the manuscript.

437

438 **Competing interests**

439 The authors declare no conflict of interest.

440 **References**

- 441 Behera, S. K., and Yamagata, T.: Subtropical SST dipole events in the southern Indian Ocean, *Geophys. Res. Lett.*,  
442 28, 327–330, <https://doi.org/10.1029/2000GL011451>, 2001.
- 443 Bey, I., Jacob, D. J., Yantosca, R. M., Logan, J. A., Field, B., Fiore, A. M., Li, Q., Liu, H., Mickley, L. J., and  
444 Schultz, M.: Global modeling of tropospheric chemistry with assimilated meteorology: Model description and  
445 evaluation, *J. Geophys. Res.*, 106, 23073–23095, <https://doi.org/10.1029/2001JD000807>, 2001.
- 446 Chen, Z. Y., Zhuang, Y., Xie, X. M., Chen, D. L., Cheng, N. L., Yang, L., and Lia, R. Y.: Understanding long-  
447 term variations of meteorological influences on ground ozone concentrations in Beijing During 2006–2016,  
448 *Environ. Pollut.*, 245, 29–37, <https://doi.org/10.1016/j.envpol.2018.10.117>, 2019.
- 449 Gelaro, R., McCarty, W., Suarez, M. J., Todling, R., Molod, A., Takacs, L., Randles, C. A., Darmenov, A.,  
450 Bosilovich, M. G., Reichle, R., Wargan, K., Coy, L., Cullather, R., Draper, C., Akella, S., Buchard, V., Conaty, A.,  
451 da Silva, A. M., Gu, W., Kim, G. K., Koster, R., Lucchesi, R., Merkova, D., Nielsen, J. E., Partyka, G., Pawson, S.,  
452 Putman, W., Rienecker, M., Schubert, S. D., Sienkiewicz, M., and Zhao, B.: The Modern-Era Retrospective Analysis  
453 for Research and Applications, Version 2 (MERRA2), *J. Climate*, 30, 5419–5454, [https://doi.org/10.1175/jcli-d-](https://doi.org/10.1175/jcli-d-160758.1)  
454 160758.1, 2017.
- 455 Good, S. A., Martin, M. J., and Rayner, N. A.: EN4: quality controlled ocean temperature and salinity profiles and  
456 monthly objective analyses with uncertainty estimates, *J. Geophys. Res. Oceans*, 118, 6704–  
457 6716, <https://doi.org/10.1002/2013JC009067>, 2013.
- 458 Han, H., Liu, J., Shu, L., Wang, T. J., and Yuan, H. L.: Local and synoptic meteorological influences on daily  
459 variability in summertime surface ozone in eastern China, *Atmos. Chem. Phys.* 20, 203–222,  
460 <https://doi.org/10.5194/acp-20-203-2020>, 2020.
- 461 Han, J. P., and Zhang, R. H.: The Dipole Mode of the Summer Rainfall over East China during 1958–2001, *Adv.*  
462 *Atmos. Sci.*, 26, 727–735, <https://doi.org/10.1007/s00376-009-9014-6>, 2009.
- 463 Holtslag, A. and Boville, B. A.: Local versus nonlocal boundary layer diffusion in a global climate model, *J.*  
464 *Climate*, 6, 1825–1842, [https://doi.org/10.1175/1520-0442\(1993\)006<1825:LVNBLD>2.0.CO;2](https://doi.org/10.1175/1520-0442(1993)006<1825:LVNBLD>2.0.CO;2), 1993.
- 465 Jia, X. L., and Li, C. Y.: Dipole oscillation in the Southern Indian Ocean and its impacts on climate, *Chinese J.*  
466 *Geophys.*, 48, 1323–1335, <https://doi.org/10.1002/cjg2.780>, 2013.
- 467 Kay, J. E., Deser, C., Phillips, A., Mai, A., Hannay, C., Strand, G., Arblaster, J., Bates, S., Danabasoglu, G.,  
468 Edwards, J., Holland, M., Kushner, P., Lamarque, J.-F., Lawrence, D., Lindsay, K., Middleton, A., Munoz, E.,  
469 Neale, R., Oleson, K., Polvani, L., and Vertenstein, M.: The Community Earth System Model (CESM) Large  
470 Ensemble Project: A community resource for studying climate change in the presence of internal climate  
471 variability, *B. Am. Meteorol. Soc.*, 96, 1333–1349, <https://doi.org/10.1175/BAMS-D-13-00255.1>, 2015.
- 472 Li, H. X., Sun, B., Zhou, B. T., Wang, S. Z., Zhu, B. Y., and Fan, Y.: Effect of the Barents Sea ice in March on the  
473 dipole pattern of air temperature in August in eastern China and the corresponding physical mechanisms, *Trans*  
474 *Atmos Sci*, 44, 89–103, <https://doi.org/10.13878/j.cnki.dgkxxb.20130427001>, 2021.

475 Li, K., Jacob, D.J., Liao, H., Zhu, J., Shah, V., Shen, L., Bates, K. H., Zhang, Q., and Zhai, S. X.: A two-pollutant  
476 strategy for improving ozone and particulate matter air quality in China, *Nat. Geosci.*, 12, 906–910,  
477 <https://doi.org/10.1038/s41561-019-0464-x>, 2019.

478 Li, S. P., Wei, H., and Feng, G. L.: Atmospheric Circulation Patterns over East Asia and Their Connection with  
479 Summer Precipitation and Surface Air Temperature in Eastern China during 1961–2013, *J Meteorol Res*, 32, 203–  
480 218, <https://doi.org/10.1007/s13351-018-7071-4>, 2018.

481 Li, Z. Q., and Xiao, Z. N.: Thermal contrast between the Tibetan Plateau and tropical Indian Ocean and its  
482 relationship to the South Asian summer monsoon, *Atmos Ocean Sci Lett*, 14, 100002,  
483 <https://doi.org/10.1016/j.aosl.2020.100002>, 2021.

484 Liao, H., Chen, W. T., and Seinfeld, J. H.: Role of climate change in global predictions of future tropospheric  
485 ozone and aerosols, *J. Geophys. Res.-Atmos.*, 111, D12304, <https://doi.org/10.1029/2005JD006852>, 2006.

486 Liu, H. L., Zhang, M. G., and Han, X.: A review of surface ozone source apportionment in China, *Atmos Ocean*  
487 *Sci Lett*, 13, 470–484, <https://doi.org/10.1080/16742834.2020.1768025>, 2020.

488 Liu, L., Guo, J. P., Chen, W., Wu, R. G., Wang, L., Gong, H. N., Liu, B., Chen, D. D., and Li, J.: Dominant  
489 Interannual Covariations of the East Asian-Australian Land Precipitation during Boreal Winter, *J. Climate*, 32,  
490 3279–3296, <https://doi.org/10.1175/JCLI-D-18-0477.1>, 2019.

491 Lin, Z. D., and Li, F.: Impact of interannual variations of spring sea ice in the Barents Sea on East Asian rainfall  
492 in June, *Atmos Ocean Sci Lett*, 11, 275–281, <https://doi.org/10.1080/16742834.2018.1454249>, 2018.

493 Lu, X., Zhang, L., Chen, Y., Zhou, M., Zheng, B., Li, K., Liu, Y., Lin, J., Fu, T.-M., and Zhang, Q.: Exploring  
494 2016–2017 surface ozone pollution over China: source contributions and meteorological influences, *Atmos. Chem.*  
495 *Phys.*, 19, 8339–8361, <https://doi.org/10.5194/acp-19-8339-2019>, 2019.

496 North, G. R., Bell, T. L., Cahalan, R. F., and Moeng, F. J.: Sampling errors in the estimation of empirical  
497 orthogonal functions *Mon. Weather Rev.*, 110, 699–706, [https://doi.org/10.1175/1520-0493\(1982\)110<0699:SEITEO>2.0.CO;2](https://doi.org/10.1175/1520-0493(1982)110<0699:SEITEO>2.0.CO;2), 1982.

499 Pu, X., Wang, T. J., Huang, X., Melas, D., Zanis, P., Papanastasiou, D. K., and Poupkou, A.: Enhanced surface  
500 ozone during the heat wave of 2013 in yangtze river delta region, china, *Sci. Total Environ.*, 603, 807–  
501 816, <https://doi.org/10.1016/j.scitotenv.2017.03.056>, 2017.

502 Rayner, N. A., Parker, D. E., Horton, E. B., Folland, C. K., Alexander, L. V., Rowell, D. P., Kent, E. C., and Kaplan,  
503 A.: Global analyses of sea surface temperature, sea ice, and night marine air temperature since the late nineteenth  
504 century, *J. Geophys. Res.*, 108, 4407, <https://doi.org/10.1029/2002JD002670>, 2003.

505 Rider, C. F., and Carlsten, C.: Air pollution and DNA methylation: effects of exposure in humans, *Clin Epigenetics*,  
506 11, 131, <https://doi.org/10.1186/s13148-019-0713-2>, 2019.

507 Sardeshmukh, P. D., and Hoskins, B. J.: The generation of global rotational flow by steady idealized tropical  
508 divergence, *J. Atmos. Sci.*, 45, 1228–1251, [https://doi.org/10.1175/1520-0469\(1988\)045<1228:TGOGRF>2.0.CO;2](https://doi.org/10.1175/1520-0469(1988)045<1228:TGOGRF>2.0.CO;2), 1988.

510 Takaya, K., and Nakamura, H.: A Formulation of a Phase-Independent Wave-Activity Flux for Stationary and  
511 Migratory Quasigeostrophic Eddies on a Zonally Varying Basic Flow, *J. Atmos. Sci*, 58, 608-627,  
512 [https://doi.org/10.1175/1520-0469\(2001\)058<0608:AFOAPI>2.0.CO;2](https://doi.org/10.1175/1520-0469(2001)058<0608:AFOAPI>2.0.CO;2), 2001.

513 Tian, B, and Fan, K.: Climate prediction of summer extreme precipitation frequency in the Yangtze River valley  
514 based on sea surface temperature in the southern Indian Ocean and ice concentration in the Beaufort Sea, *Int. J.*  
515 *Climatol*, 40, 4117–4130, <https://doi.org/10.1002/joc.6446>, 2019.

516 Wang, H, and He, S.: The North China/northeastern Asia severe summer drought in 2014, *J. Climate*, 28, 6667–  
517 6681, <https://doi.org/10.1175/JCLI-D-15-0202.1>, 2015.

518 Wang, J, and Guo, Y.: Possible impacts of Barents Sea ice on the Eurasian atmospheric circulation and the rainfall  
519 of East China in the beginning of summer, *Adv Atmos Sci*, 21, 662-674, <https://doi.org/10.1007/BF02915733>,  
520 2004.

521 Xia, S. W., Yin, Z. C., and Wang, H. J.: Remote Impacts from Tropical Indian Ocean on January Haze Pollution  
522 over the Yangtze River Delta, *Atmos Ocean Sci Lett*, 14, 100042, <https://doi.org/10.1016/j.aosl.2021.100042>,  
523 2021.

524 Xu, H. W., Chen, H. P., and Wang, H. J.: Interannual variation in summer extreme precipitation over Southwestern  
525 China and the possible associated mechanisms, *Int J Climatol*. 41, 3425–3438, <https://doi.org/10.1002/joc.7027>,  
526 2021.

527 Xu, W. Y., Xu, X. B., Lin, M. Y., Lin, W. L., Tarasick, D., Tang, J., Ma, J. Z., and Zheng, X. D.: Long-term trends  
528 of surface ozone and its influencing factors at the Mt Waliguan GAW station, China – Part 2: The roles of  
529 anthropogenic emissions and climate variability, *Atmos. Chem. Phys.*, 18, 773–798, [https://doi.org/10.5194/acp-](https://doi.org/10.5194/acp-18-773-2018)  
530 18-773-2018, 2018.

531 Yang, Y., Liao, H., and Li, J.: Impacts of the East Asian summer monsoon on interannual variations of summertime  
532 surface-layer ozone concentrations over China, *Atmos. Chem. Phys.*, 14, 6867–6879, [https://doi.org/10.5194/acp-](https://doi.org/10.5194/acp-14-6867-2014)  
533 14-6867-2014, 2014.

534 Yin, Z. C., and Ma, X. Q.: Meteorological Conditions Contributed to Changes in Dominant Patterns of Summer  
535 Ozone Pollution in Eastern China, *Environ. Res. Lett.*, 15, 124062, <https://doi.org/10.1088/1748-9326/abc915>,  
536 2020.

537 Yin, Z. C., Wang, H. J., Li, Y. Y., Ma, X. H., and Zhang, X. Y.: Links of Climate Variability among Arctic sea ice,  
538 Eurasia teleconnection pattern and summer surface ozone pollution in North China, *Atmos. Chem. Phys.*, 19,  
539 3857–3871, <https://doi.org/10.5194/acp-19-3857-2019>, 2019.

540 Zhao, Z. J., and Wang, Y. X.: Influence of the west pacific subtropical high on surface ozone daily variability in  
541 summertime over eastern China, *Atmos. Environ.*, 170, 197–204, <https://doi.org/10.1016/j.atmosenv.2017.09.024>,  
542 2017.

543 Zhou, D. R., Ding, A. J., Mao, H. T., Fu, C. B., Wang, T., Chan, L. Y., Ding, K., Zhang, Y., Liu, J., Lu, A., and  
544 Hao, N.: Impacts of the East Asian monsoon on lower tropospheric ozone over coastal South China, *Environ. Res.*  
545 *Lett.*, 8, 044011, <https://doi.org/10.1088/1748-9326/8/4/044011>, 2013.

546 **Table and Figure captions**

547 **Figure 1.** (a) Spatial distributions of observed (dots) and GEOS-Chem simulated (shading) summer-mean MDA8  
548 O<sub>3</sub> (unit:  $\mu\text{g m}^{-3}$ ) for the period 2015–2019. (b) The second EOF spatial pattern of simulated summer-mean MDA8  
549 O<sub>3</sub> from 1980 to 2019. The simulated O<sub>3</sub> concentrations were produced by GEOS-Chem with fixed emissions but  
550 changing meteorological conditions from 1980 to 2019. The green boxes represent the areas of NC and the PRD.

551 **Figure 2.** Variations in standardized DP-O<sub>3</sub> time series (black), May SI near the Franz Josef Land (SI<sub>FJL</sub>, red),  
552 January–February–March mean Subtropical Indian Ocean Dipole (SIOD, blue), and SEI (green) from 1980 to  
553 2019. SEI defined as the weighted average of SI<sub>FJL</sub> and SIOD. The correlation coefficients of the DP-O<sub>3</sub> with SI<sub>FJL</sub>  
554 (red), SIOD (blue), and SEI (green) were shown in the figure.

555 **Figure 3.** Composite summer atmospheric circulations associated with the DP-O<sub>3</sub> (DP-O<sub>3</sub>P minus DP-O<sub>3</sub>N) for  
556 the period 1980 to 2019, including (a) surface air temperature (SAT, unit: K, shadings) and geopotential height at  
557 500 hPa (unit: 10 gpm, contours), (b) surface incoming shortwave flux (Ssr, unit:  $\text{W m}^{-2}$ , shadings) and low and  
558 medium cloud cover (Mlcc, unit: 1, contours), and (c) precipitation (Prec, unit: mm, shadings) and surface wind  
559 (unit:  $\text{m s}^{-1}$ , arrows). The white dots indicate that the composites with shading were above the 90% confidence  
560 level. The black boxes in (a) indicate the centers of the AC<sub>NC</sub> and C<sub>PRD</sub>, respectively. The green boxes in (b) and  
561 (c) represent the areas of NC and the PRD. Composites of the summer mass fluxes of O<sub>3</sub> (d) associated with the  
562 DP-O<sub>3</sub> (DP-O<sub>3</sub>P minus DP-O<sub>3</sub>N) for the area-averaged differences (NC minus PRD) from 1980 to 2019. The  
563 bottom axis gives the names of the chemical and physical processes: chemical reaction (Chem), convection (Conv),  
564 PBL mixing (Mix), transport (Trans) and their sum (Sum).

565 **Figure 4.** Composites of (a) May SI concentration and (b) JFM SST associated with the DP-O<sub>3</sub> (DP-O<sub>3</sub>P minus  
566 DP-O<sub>3</sub>N) from 1980 to 2019. The green boxes in (a) and (b) indicate where the SI<sub>FJL</sub> and SIOD indices are  
567 calculated, respectively. The white dots indicate that the composites were above the 90% confidence level.  
568 Composite summer meteorological conditions, circulations and mass fluxes of O<sub>3</sub> associated with (c) SI<sub>FJL</sub>  
569 (positive SI<sub>FJL</sub> years minus negative SI<sub>FJL</sub> years) and (d) SIOD (positive SIOD years minus negative SIOD years)  
570 from 1980 to 2019. The bottom axis gives the names of the meteorological conditions and chemical and physical  
571 processes: the differences between AC<sub>NC</sub> and C<sub>PRD</sub> (unit: 10 gpm), surface incoming shortwave flux (Ssr, unit:  $\text{W}$   
572  $\text{m}^{-2}$ ), surface air temperature (SAT, unit: K), and precipitation (Prec, unit: mm); chemical reaction (Chem, unit:  
573  $\text{Tons d}^{-1}$ ), convection (Conv, unit:  $\text{Tons d}^{-1}$ ), PBL mixing (Mix, unit:  $\text{Tons d}^{-1}$ ), transport (Trans, unit:  $\text{Tons d}^{-1}$ )  
574 and their sum (Sum, unit:  $\text{Tons d}^{-1}$ ).

575 **Figure 5.** Composites of (a) May Arctic SST (unit: K), (c) velocity potential (unit:  $10^5 \text{ m}^2 \text{ s}^{-1}$ , shading) and  
576 divergent wind at 500 hPa (unit:  $\text{m s}^{-1}$ , arrows), and (e) Rossby wave source anomalies at 500 hPa (unit:  $10^{-11} \text{ s}^{-2}$ )  
577 associated with SI<sub>FJL</sub> index (negative SI<sub>FJL</sub> years minus positive SI<sub>FJL</sub> years) from 1980 to 2019. The back box in  
578 (a) and (b), yellow box in (c) and (e) and green box in (d) and (f) represents the center of the SST, velocity potential  
579 and Rossby wave source anomaly associated with SI<sub>FJL</sub>, respectively. The white dots indicate that the composites  
580 with shading were above the 90% confidence level.

581 **Figure 6.** Composites of (a) wave activity flux anomalies (unit:  $\text{m}^2 \text{ s}^{-2}$ , arrows), geopotential height (unit: gpm,  
582 shading) at 500 hPa and (b) mean wind (unit:  $\text{m s}^{-1}$ , arrows), omega (unit:  $10^{-2} \text{ Pa s}^{-1}$ , shading) over 100–130° E,  
583 and the anomalies of AC<sub>NC</sub> and C<sub>PRD</sub> (unit: gpm, bar) in summer associated with SI<sub>FJL</sub> index (negative SI<sub>FJL</sub> years



584 minus positive  $SI_{FJL}$  years) from 1980 to 2019. The green boxes in (a) represent the centers of the EU-like pattern.  
585 The white dots indicate that the composites with shading were above the 90% confidence level.

586 **Figure 7.** Composite differences of geopotential height at 500 hPa in JJA between three low and high  $SI_{FJL}$  years  
587 based on the ensemble of 40 CESM-LE simulations during 1980–2019. The black dots indicate that the  
588 mathematical sign of the composite results of more than 60% of the members is consistent with the ensemble  
589 mean. The black boxes represent the centers of the EU-like pattern.

590 **Figure 8.** (a) Composites of mean 0–60m subsurface ocean temperature (unit: K) in summer associated with the  
591 SIOD (positive SIOD years minus negative SIOD years) from 1980 to 2019. The green boxes represent the centers  
592 of the SIOD, and the black box indicates where the SOT index is calculated. Composites of (b) OLR (unit:  $W m^{-2}$ )  
593 and (c) velocity potential (unit:  $10^5 m^2 s^{-1}$ , shadings) and divergent winds (unit:  $m s^{-1}$ , vectors) at 10 m in summer  
594 associated with SOT indexes of opposite sign (negative SOT years minus positive SOT years). The black box  
595 represents the center of the SOT. (d) Composites of summer mean winds (unit:  $m s^{-1}$ , arrows) and omega (unit:  
596  $10^{-2} Pa s^{-1}$ , shadings) over  $90\text{--}120^\circ E$ , and the anomalies of  $AC_{NC}$  and  $C_{PRD}$  (unit:  $gpm$ , bars) associated with SOT  
597 indexes of opposite sign. The white dots indicate that the composites with shading were above the 90% confidence  
598 level.

599 **Figure 9.** Composite differences of geopotential height at 500 hPa in JJA between three high and low SIOD years  
600 based on the ensemble of 40 CESM-LE simulations during 1980–2019. The black dots indicate that the  
601 mathematical sign of the composite results of more than 60% of the members is consistent with the ensemble  
602 mean. The black boxes represent the centers of  $AC_{NC}$  and  $C_{PRD}$ , respectively.

603 **Figure 10.** Schematic diagrams of the associated physical mechanisms. The May SI anomalies near the Franz  
604 Josef Land (red shadings) could trigger an EU-like pattern in the atmosphere in summer, which enhances the  
605 anticyclonic anomaly over NC and the cyclonic anomaly over the PRD. The thermodynamic signal of the  
606 preceding SIOD (contours) could be stored in the subsurface and the center of negative SST anomalies moves to  
607 the vicinity of Sumatra Island in summer (blue shading). The meridional circulation was enhanced in summer  
608 (dashed lines), along with the enhancement of  $AC_{NC}$  and  $C_{PRD}$  over eastern China. The solid lines indicate the  
609 anomalous atmospheric circulations affected by  $SI_{FJL}$ , while the dashed lines indicate the anomalous atmospheric  
610 circulations affected by SIOD.

611 **Figure 11.** (a) Composites of geopotential height at 500 hPa (unit:  $gpm$ , shadings) in summer associated with the  
612 SEI (positive SEI years minus negative SEI years) from 1980 to 2019. The red and blue lines indicate areas where  
613 the composite geopotential height anomalies associated with  $SI_{FJL}$  and SIOD exceed the 90% confidence level,  
614 respectively. The black boxes represent the centers of  $AC_{NC}$  and  $C_{PRD}$ , respectively. (b) Composite differences of  
615 the detrended summer-mean MDA8  $O_3$  (unit:  $\mu g m^{-3}$ ) simulated by GEOS-Chem model between high and low  
616 SEI years during 1980–2019. The white dots indicate that the composite differences are above the 90% confidence  
617 level. The green boxes represent the areas of NC and the PRD.

618